Insights into the seismogenic structures of the arc-continent convergent boundary in eastern Taiwan

W.S. Chen (1), Y.M. Wu (1, 2), P.Y. Yeh (1), Y.X. Lai (3), S.S. Ke (3), M.C. Ke (3)

1. Department of Geosciences, National Taiwan University, Taipei 10617, Taiwan
2. Institute of Earth Sciences, Academia Sinica, Taipei 11529, Taiwan
3. National Science and Technology Center for Disaster Reduction

Wenshan@ntu.edu.tw
drymwu@ntu.edu.tw
boyi6030@gmail.com
monk112358@hotmail.com
opbook@ncdr.nat.gov.tw
mcke@ncdr.nat.gov.tw

Abstract

Taiwan's doubly vergent orogen is a relatively young and active arc-continent collision caused by the convergence of the Eurasian and Philippine Sea Plates occurring along a complicated seismogenic plate boundary. This study aims to investigate the evolutionary and tectonic features of the retro-wedge, which is involved in uplifting and shortening the growth of the Taiwan orogen. We delineate three potential seismogenic structures: the Longitudinal Valley Fault (LVF), the Ludao–Lanyu Fault (LLF), and the Central Range Fault (CRF) along the convergent boundary by using seismic tomographic image and relocated seismicity. We first discovered a west-dipping backthrust of the CRF bounding on the eastern Backbone Range, which can be traced to a distance of 300 km from the north Hualien city to the southeastern offshore. The fault led to the development of a crustal scale pop-up structure and resulted in the formation of a doubly vergent orogenic wedge in the retro-wedge side. Thus, the generation of the basement-involved backthrust has been attributed to the indentation of the exhumed forearc mantle wedge and remnant forearc crust into the Backbone Range during collision. As a result, the plate boundary consists of two opposite vergent thrust systems of the LVF–LLF and CRF that developed during the collision, following the closure of the forearc basin of the North Luzon Trough and Longitudinal Valley from incipient to mature collision, respectively. Our results provide new tectonic features along convergent zone constraints for geodynamic models of arc-continent collision allowing investigations of current mountain building in Taiwan.

Key words: doubly vergent orogen, seismogenic structure, indentation, the Longitudinal Valley Fault, the Backbone Range, arc-continent collision

1. Introduction

Due to the ongoing arc-continent collision, the island of Taiwan occurs a relatively young and active orogenic belt, displaying a complicated and dynamic convergent plate boundary between the Philippine Sea (PSP) and the Eurasian (EU) Plates. In particular, Taiwan is located at the flipping location of the subduction polarity reversal between the Ryukyu and Manila Trenches (Suppe, 1984). The plate boundary is considered a natural laboratory for studying the mechanism of mountain building due to the continuous arc-continent collision. The relocated seismicity and seismic tomography for crust structure beneath Taiwan and the surrounding offshore area have been previously discussed, such as the northern (Ryukyu Trench) and southern (Manila Trench) subduction zones (Rau and Wu, 1995; Chemenda et al., 1997; Kao and Jian, 2001; Lin et al., 2004; Wang et al., 2004; Wu et al., 2009a, b; Ustaszewski et al., 2012; Lallemand et al., 2013; Chen et al., 2013, 2017a; Huang et al., 2014), the mountain "root" structure under the Backbone Range (Rau and Wu, 1995; Lin et al., 1998; Kim et al, 2005, 2006; Wu et al., 2007, 2014; Kuo-Chen et al., 2012; Lallemand et al., 2013; Huang et al., 2014), and the PSP/EU collision boundary in the Longitudinal Valley (Kim et al., 2005, 2006; Liang et al., 2007; Cheng, 2009; Kuo-Chen et al., 2009, 2012; Wu et al., 2014). Even though the lithospheric scale seismicity clearly delineates the collision and subduction tectonic features, there is still insufficient information for analyzing the structure of the arc-continent convergent boundary or different views. The doubly vergent wedge models need a backthrust at the retroside to explain the evolution of the orogen (e.g. Malavieille et al., 2002; Willett and Brandon, 2002; Willett et al., 2003; Malavieille and Trullenque, 2009; Malavieille and Konstantinovskaya, 2010). In previous studies, no definitive evidence showed that a backthrust (the Central Range Fault) exists along the retro-wedge side, however, the existence of the Central Range Fault (CRF) has been since further discussions. It was only a conceptual model without solid geophysical data to support. Therefore, this study can provide important insight into the mechanical model for Taiwan's doubly vergent orogen and even global orogens.

The diachronous uplift of Taiwan's orogen suggests a tendency for a progressively southward oblique arc-continent collision (Suppe, 1984; Teng, 1990). This collision was accompanied by successive forearc basin closure (Huang et al., 1992) and cessations in the North Luzon Arc (NLA) magmatism (Shao et al., 2015). Thus, more complicated structures along the plate boundary do not provide much detail (Figure 1). For example, we do not know whether a west-dipping (eastward vergent) backthrust (CRF) exists beneath the eastern Backbone Range in the retro-wedge province, whether the collision has caused an indentation of a remnant forearc crust under the Longitudinal Valley, or what changes exist in the structural features from the subduction-collision transitional zone to the collision zone.

Recently, 3-D seismic velocity structures have been well determined in Taiwan (Huang et al., 2014) and the earthquake catalog has also been relocated using a 3-D model (Wu et al., 2007, 2008a, 2008b, 2009). This motivated us to determine the seismogenic structures of the convergent boundary in eastern Taiwan. We systematically investigated a series of comprehensive seismic tomographic transects associated with the determination of focal mechanisms, and relocated seismicity to delineate the major seismogenic structures, compared with geological observations, to constrain tectonic settings. Earthquake focal mechanism solutions for the stress inversion are particularly important to understand the properties of active faults and regional tectonics throughout a complex convergent zone. In this study, we also attempted to estimate stress fields from focal mechanisms in each seismogenic zone.

2. Tectonic Setting

Taiwan's orogeny was caused by an arc-continent collision between the EU and PSP Plates, occurring in the late Miocene. Afterwards, the collided PSP in the western edge became a northward subduction under the EU, occurring in the middle of the Pleistocene period. The junction of the Ryukyu-Manila Trench displays a flipping structure of the LVF in east Taiwan (Suppe, 1984). This widely recognized plate boundary on land is along the LVF, which separates two major tectonic provinces of the Coastal Range to the east and the Backbone Range to the west (Figure 1). West of the LVF, the Backbone Range mainly consists of Eocene-Miocene high-pressure metamorphic rocks from the Yuli belt that underwent subduction during the middle of the Miocene and were then exhumed in the late-middle Miocene (Chen et al., 2017b). The Coastal Range represents a middle Miocene-Pliocene volcanic arc, which has been overridden onto the Backbone Range during the Pliocene (Chen and Wang, 1988).

Geological maps, GPS surveys, and historical earthquake ruptures capturing the seismic activity along the LVF have been utilized to outline the most obvious surface expressions to point out the exact location in the Longitudinal Valley (Wang and Chen, 1997; Shyu et al., 2006; Chen et al., 2007). Through relocated seismicity and tomography investigations that were restricted to the fault geometry (depth ~50 km), it was determined that there is an east-dipping high-angle seismogenic zone developing under the Coastal Range (Rau and Wu, 1998; Kuo-Chen et al., 2004, 2012).

The diachronous orogenic uplift from the late Miocene suggests an asymmetric exhumation and erosion of the orogenic wedge over time, due to oblique collision (Willett et al., 2003; Liu et al., 2000; Chen et al., 2019). During orogeny, compressional deformation and erosion appears to result in different burial depths of rocks exposed at the ground surface over the orogenic belt. Three tectonic provinces of orogen can be distinguished by rock type: stratigraphic, structural, and metamorphic characteristics of the Backbone Range, Hsuehshan Range, and Western Foothills from east to west, respectively (Figure 1). These characteristics result in the progressive eastward propagation of mountain building (Chen et al., 2019). On the basis of stratigraphy and mesoscopic semi-ductile deformation in the Backbone Range, it appears that the shortening has been generated to achieve a large-scale anti-form of Neogene pop-up fold (Yen, 1967). A west-dipping backthrust bounding the eastern margin of the Backbone Range, namely the Central Range Fault (Biq, 1965; Ho, 1986), was proposed in order to further explain the crustal structure of the doubly vergent orogen (Willett et al., 2003; Shyu et al., 2006; Malavieille and Konstantinovskaya, 2010).

As in east Taiwan, the seismic tomography shows the deep crustal structures, which were obtained from the two subduction zones, the eastward subduction of EU under the PSP in the southeastern offshore and the northward subduction of PSP under the EU in the eastern offshore (Rau and Wu, 1995; Chemenda et al., 1997; Kao and Jian, 2001; Lin et al., 2004; Wu et al., 2009a, b; Ustaszewski et al., 2012; Lallemand et al., 2013; Chen et al., 2013, 2017a; Huang et al., 2014). The collision zone of the LVF reveals a link between the Ryukyu and Manila subduction zones.

3. Data

In this study, the 3-D seismic velocity model from Huang et al. (2014a, b) was used. It is the latest velocity model in the Taiwanese region. This velocity model is determined by the joint inversion of local, regional, and teleseismic data. Arrivals of the teleseismic events are recorded from Taiwan's seismic network. P and S arrivals of the local seismic events are recorded by Taiwan's and the Ryukyu Islands' seismic network. Local S-P time differences recorded by Taiwan Strong Motion Instrument Program (TSMIP; about 800 stations) are used for tomography inversion to provide better constraints on Vp/Vs inversion. P and S arrivals from temporary ocean bottom seismometers around Taiwan are also used for tomography inversion. Tomography inversion enhances the resolution for offshore regions especially for the eastern offshore of Taiwan. Logging P- and S-wave velocities in shallowest 30-60 meters at 445 drilling sites of the TSMIP stations over the Island provides valuable and accurate information of near-surface velocity structures (Kuo et al., 2012b) for near-surface correction in tomographic inversion process.

A seismic catalog and focal mechanisms from 1990 to 2018 by Wu et al. (2008a, b) were used in this study. This catalog includes 679,986 events that were relocated using 3-D velocity structures with station correction (Wu et al., 2003), P and S arrivals from Taiwan's and the Ryukyu Islands' seismic network, and S-P time differences recorded by TSMIP. After the relocation using the 3D model with the station corrections, the travel-time residuals have the means and standard deviations of -0.006 ± 0.313, -0.004 ± 0.455, and 0.029 ± 0.365 sec for P, S, and S-P data, respectively, a significant reduction in the travel-time residuals (Wu et al., 2008a). Wu et al. (2013) used signals from ten explosions to examine earthquake location uncertainty of the relocated catalog. For the inland earthquakes, location errors in longitude, latitude, and depth were approximately 3.1±2.7, 1.3±1.6, and 4.6±3.9 km, respectively. Totally, 10,448 focal mechanisms were determined using the first P polarities from the relocated seismic catalog (Wu et al., 2008b, 2010). For this focal mechanism catalog is well determined. Quality index of all determined focal mechanisms (defined by Wu et al., 2008b) should be large than 0.1. In general, all of the focal mechanisms have more than 10 readings with both up and down polarity, polarities fitness large than 70%, and station coverage gap less than 180˚. The data used in this study will provide a comprehensive archive for detailed seismological and tectonic investigations in the Taiwan region.

4. Results and Discussions

The seismicity in eastern Taiwan extends along the convergent plate boundary. In this study, we investigated the tectonic structures of the collision zone from tomographic 3-D models of Vp, Vp/Vs, and Vs perturbation structures and combined them with relocated earthquakes and focal mechanisms. We constructed thirteen vertical seismic tomography transects with a 120 km width along the oriented N70°W (transects 1–10) and places the E–W (transects 11–13) approximately perpendicular to the convergent plate boundary. This allowed us to further show crustal structures from the northern Hualien city to the southeastern offshore area (latitude 22°00`–24°30`N; Figure 1). To better understand the links between tectonic structures and seismicity, this study has identified three tectonic regimes in eastern Taiwan, including: (a) the Ryukyu Trench subduction zone at the westernmost edge of PSP (Figure 1, A area), (b) the collision zone at the Longitudinal Valley (B area), (c) the collision-subduction transition zone at the southeastern offshore (C area).

However, before describing the tectonic features of the convergent zone, we infer the Vp velocity and Vp/Vs values from previous studies that defined crustal structures. Thus, we assumed a continuous contour of Vp =7.5 km/s to constrain the Moho interface depth (Kuo-Chen et al., 2012; Ustaszewski et al., 2012; Van Arendonk et al., 2014), which roughly coincided with the Vp/Vs value of 1.75 ± 0.1 (Lombardi et al., 2008). In addition, we postulated a thickness of 8–11 km for the PSP in the western Philippine Sea (Wang et al., 2004), which is overlain by a 3-5 km thick pile of sediments (Malavieille et al., 2002). We estimated that the depth of the top of the oceanic crust (PSP) is about 6–8 km in the eastern offshore area by using seismic reflection (Malavieille et al., 2002) and velocity data (White et al., 1992; Wang et al., 2004). Due to poor seismic station coverage in the eastern offshore region, we have a low resolution of data for the crustal structures in the easternmost transects.

4.1 The collision-subduction transition zone at Taiwan's southeastern offshore

The South China Sea oceanic slab is presently sliding eastward under the PSP at the Manila Trench with developments of the North Luzon Arc (NLA) and North Luzon Trough (NLT, forearc basin), and the Backbone Range/Hengchun Peninsula (accretionary wedge) (Figure 1). Seismic tomography is unable to achieve a better resolution of deep seismic imagery in the southern transects, however, relocated earthquakes have shown the subduction slab dipping ~60° eastward to a maximum depth of 150 km (Figure 2, transects 10–13). North of Taitung city (latitude 22°45`N), there seems to be a cease of activity from earthquakes along the subduction zone.

The NLT is located between the Backbone Range and NLA (Figure 1). The seismic tomographic images reveal an anomalously high velocity layer, exhibiting high Vp and low Vp/Vs beneath the NLT at 8–20 km depth (Figure 2, transects 11–13). This most likely indicates the existence of a forearc crust. In addition, this region consists of an ~8 km thick deposits of basin-fill sequence and a deformed accretionary wedge determined by a seismic reflection investigation (Malavielle et al., 2002; McIntosh et al., 2005; Hirtzel et al., 2009). Our tomographic images also exhibited a reduced Vp, negative Vs perturbation, and high Vp/Vs (Wu et al., 2007). However, the NLT reveals thick sedimentary deposits overlying a remnant forearc crust, or retro-foreland basin (Huang et al., 1992).

We investigated the seismicity in southeastern Taiwan which revealed the presence of two significant but opposite dipping seismogenic zones on either side of the NLT. East of the east-dipping seismogenic zone (marked in (d), Figure 2, transects 10–13), located in front of the NLA and to the south from the Ludao (latitude 22°40'N) to Lanyu Islands at least, focal mechanism solutions from 35 data points (79.5%) show the principal compression axes (P-axes) orientation with an azimuth range 280–300° by reverse and oblique-reverse (other) events (Figures 3 (area-6), 4g, and 5c). Our seismic tomographic model is rife with inaccuracies, specifically east of the LZA due to poor seismic stations that were distributed in the far eastern region. However, seafloor geomorphic expressions revealed a significant lineament of a scarp feature along the fault tip of the seismogenic zone, namely the Ludao–Lanyu Fault (LLF) (Chen et al., 2019).

Another seismogenic zone (marked in (a), Figures 1 and 2, transects 11–13) in the west, between the Backbone Range and NLT, is also observed in the seafloor geomorphic expression and forms a scarp feature. Using relocated earthquakes, it was determined that this feature occurs in a west-dipping seismogenic zone at depths shallower than 15 km. In addition, the Vp/Vs ratio can provide the information on the lithological property and pore fluid content; thus, high Vp/Vs values are expected in failed fractures and water-saturated rocks (Baris et al., 2005). Our tomographic images show that the metamorphic belt of the Backbone Range has a lower Vp/Vs and higher Vs perturbation than the NLT of the basin-fill sequence. The resulting laterally heterogeneous seismic velocity structures can be clearly defined as significant west-dipping boundaries, coinciding with the seismicity data, which occur in a seismogenic zone. Focal mechanism solutions from 64 data points (91.8%) show the P-axes orientation with the azimuth range at 290–310° by reverse, oblique-reverse (other), and strike-slip events. In addition, an eastward vergent thrusting (Figures 3 (area-4), 4e, and 5f) is also present. Further to the north, the seismogenic zone can be followed to trace the CRF on the Longitudinal Valley (marked in (a), Figures 1 and 2, transects 1–10).

The northernmost NLT becomes narrower until it closes at the Longitudinal Valley (between transects 10 and 11), which is a response to the closure of the retro-foreland basin along the two opposite dipping thrusts (Figure 6c). The southern Backbone Range and the NLA then override the retro-forearc basin. The northwestward migration and clockwise rotation of the PSP led to a cessation of volcanic activity at 1.5 Ma (Shao et al., 2015). Currently, the top of the subducting slab is located at 60–80 km beneath the NLA. Apparently, the NLT is gradually closing while the forearc crust has begun to descend into the convergent zone due to arc-continent collision.

4.2 The collision zone at the Longitudinal Valley

The Longitudinal Valley exhibited a completely closed ancient forearc basin during the middle of the Pleistocene (< 0.8 Ma) period where the Coastal Range was overthrust westward onto the Backbone Range along the LVF (Chen and Wang, 1988). The collision zone is characterized by the presence of two opposite dipping seismogenic zones with the LVF to the east and the CRF to the west, as inferred from relocated seismicity (Figure 2). Thus, it appears to inherit the tectonic structures of the collision-subduction transition zone. In this study we first define the west seismogenic zone along the collision zone (discussed further below).

4.2.1 The Longitudinal Valley Fault (LVF)

The LVF extends southward for 170 km along the Longitudinal Valley from the southern portion of Hualien city to the southern part of Taitung city (Figure 2, transects 3–10). However, no earthquakes were located in the southeastern offshore region along the fault trace, which ends immediately west of Ludao Island (latitude 22°40`N) but does not extend to the south (Figures 1 and 2, transects 11–13). The LVF is the most obvious surface expression for the junction of the Backbone Range and the Coastal Range (Chen et al., 2007; Figure 7a, 7b, 7c). In this study, we mapped and compared the tomography across the Longitudinal Valley, indicating the relatively low Vp, high Vp/Vs, and negative Vs perturbation on the LVF hanging wall (Figure 2, transects 3–10). Its characteristics reveal the presence of pore water in the sediments and sedimentary/volcanic rocks in the Coastal Range. By contrast, the LVF footwall was characterized by high Vp, low Vp/Vs, and positive Vs perturbation, which suggests that the across-fault changes cause relationships among metamorphic and sedimentary/volcanic rocks of the EU and PSP Plates, respectively. Apparently, the upper crust exhibits a different velocity structure on both sides of the LVF and LYF (Figure 2, marked in (b) and (c)). Thus, the Longitudinal Valley represents one of the most seismically active regions of Taiwan. As a result of the relocated earthquakes, the tomographic boundary, in correspondence with a cluster of small-to-moderate earthquakes, occurs in an east-dipping seismogenic zone which extends to a depth of 40–50 km. In the northern segment, the seismogenic zone dips east at 70–75° up and to 25 km depth, and 40–50° below at a 30 km depth (Figure 2, transects 3–7). Furthermore, the southern segment becomes lower with a dip of 60° and up to a 25 km depth, and 38–45° below at a 25 km depth (Figure 2, transects 8–10). The fault dip is steeper in the north and may represent a response to the progressive southward collision. Historical seismic records along the active plate boundary have recorded the most significant seismic activity, including the 1951 Taitung (Ms 6.8), 1972 Juisui (M_L 6.9), and 2003 Chengkung (Mw 6.8) earthquakes (Figure 1). Most earthquake events (94%) show a consistent pattern of P-axes orientation with the azimuth range of 290–330° by reverse, oblique-reverse (other), and strike-slip events (Figures 3, 4c, and 5c ; all of 956 data), which significantly corresponds to the direction of plate convergence determined from GPS observations (Chen et al., 2017a; Ching et al., 2011).

On the southern Longitudinal Valley, a wedge shape of high Vp/Vs and negative Vs perturbation zone exists on the LVF footwall (Figure 2, transects 6–9). Its western boundary on the ground surface follows the Luyeh fault (Figures 1 and 2, marked in (c)) that joins together with the LVF at a depth of 20–30 km (Chen et al., 2007). The Luyeh fault extends further to the north and becomes a blind fault beneath the west-dipping seismogenic zone of the CRF (Figure 2, transects 6–7; Figure 7c).

4.2.2 The Central Range Fault (CRF)

West of the Longitudinal Valley, resulting from the density of the seismic tomography transects (Figure 2, transects 3–10), we found that most compressive earthquakes follow a west-dipping seismic zone beneath the eastern Backbone Range. Previous studies combining earthquake distribution and tomography were used to illuminate crustal structures across the collision zone but have only documented the east-dipping seismogenic zone of the LVF. However, the west-dipping seismogenic zone of the CRF is often neglected (Tsai, 1986; Lin et al., 1998; Rau and Wu, 1998; Cheng and Wang, 2001; Kao and Jian, 2001; Cheng et al., 2002; Kuo-Chen et al., 2004, 2012; Chen et al., 2007). This CRF zone was well-documented by the research from the Taitung (M_W 6.1) earthquake on 04/01/2006 (Wu et al., 2006; Mozziconacci et al., 2013) and the Juisui (M_L6.3) earthquake on 10/31/2013 (Figure 1). Numerous studies have speculated that a west-dipping backthrust under the eastern Backbone Range led to the development of a crustal scale pop-up fold (e.g., Yen, 1967; Ho, 1986; Willett and Brandon, 2002; Willett et al., 2003). Therefore, few studies have attempted to investigate the CRF and have never identified it in field mapping (Ho, 1986; Shyu et al., 2005). Shyu et al. (2006) and Chen et al. (2007) all discussed the CRF in their studies with some relatively indirect proofs. In the field survey, no offset or deformation of Holocene alluvial fans was found along the Longitudinal Valley (Figure 7b and 7c). However, according to the geological drilling and shallow seismic refraction investigations, there is no evidence of surface rupture at the front of the eastern Backbone Range (Chang, 2015; Yen, 2017).

Certainly, our study from relocated earthquakes shows a well-delineated 60–72° west-dipping seismogenic zone reaching a depth of ~20 km (Figure 2, marked in (a)) beneath the eastern Backbone Range. The Backbone Range is characterized by the strong heterogeneity of Vs perturbation and Vp/Vs at a shallow depth across the seismogenic zone. This is sufficient to corroborate the existence of a CRF, which is 300 km long when measuring from the southeastern offshore to the northern Hualien city (Figure 1).

Focal mechanism solutions of 426 data points (98.6%) show P-axes orientation with the azimuth range of 300–330° by reverse, oblique-reverse (other), and strike-slip events (Figures 3, 4d, and 5f; all of 429 data), indicating that uplift of the Backbone Range is affected by a back-thrusting fault. In the past two decades, medium magnitude earthquakes often occurred along the CRF where there are no surface ruptures. Examples include the Taitung (M_W 6.1) earthquake on 04/01/2006, Juisui (M_L 6.3) earthquake on 10/31/2013, Fenglin (M_L 5.9) earthquake on 5/21/2014, and Xiulin (M_L 6.1) earthquake on 4/18/2019 (Figure 1; Wu et al., 2006; Chuang et al., 2014; Lee et al., 2014; Canitano et al., 2015; Wen et al., 2016). Based on the earthquake distributions, a seismic gap occurs between transect 7 and transect 8 (Figures 1 and 2), which may represent locked portions along the CRF. Furthermore, CRF was not found by field mapping due to a blind thrust beneath the LVF. Our seismic tomography transects showed that a fault tip appears to be blind and does not cut through the ground surface (Figure 2, transects 3–9; Figure 6b).

4.3 The Ryukyu Trench subduction zone at the westernmost edge of the Philippine Sea Plate

The north part of Hualien city is starting to experience the flipping of plate interactions from collision to northward subduction (Wu et al., 1997); consequently, more complicated tectonic structures and seismicity are occurring. Figures 1 and 2 of the tomography transects 2–3 are set up to cross the Ryukyu trench containing three different geological provinces of the Backbone Range, collision zone (plate boundary), and the westernmost Yaeyama accretionary wedge. The westernmost PSP started to subduct northward under the Backbone Range of the EU and is located around the collision-subduction transition zone. In this study, a series of tomographic transects provided that the Moho interface under the Backbone Range and shows a convex downward shape at a depth of 50–55 km with an overthickened crust (Figure 2, transects 1–11). There is also an abruptly eastward shallowing at a depth of ~30 km beneath the convergent zone.

Most moderate earthquakes (M_S>3) occurring on a west-dipping seismogenic zone can be traced to a 20 km depth (Figure 2, transects 1–3). Thus, focal mechanism solutions of 813 data points (90.9%) show P-axes orientation with the azimuth range from 300–330° by reverse and oblique-reverse (other) events (all of 895 data; Figures 3 (area-1), 4a, and 5a). This has also been revealed by the 02/06/2018 M_L 6.4 Hualien earthquake (focal mechanism P-axis 340°; Figure 1). Furthermore, this indicates that the Backbone Range is clearly bounded by an eastward vergent backthrust (marked in (a), Figure 2, transects 1–3), which is known as the CRF (Chen et al., 2018). Our tomographic images reveal a strong heterogeneity across the fault zone. Such high Vp regions with positive Vs perturbation and low Vp/Vs on the hanging wall to the west could be related to the metamorphic belt of the Backbone Range. In contrast, east of the seismogenic zone on the footwall, there is a low Vp region either negative Vs perturbation and high Vp/Vs, which is thought to be a deformed accretionary wedge of the Yaeyama Ridge and basin-fill sequence. Moreover, seismic activity has recorded a significantly different focal solution in this region. Most moderate earthquakes (M_S>3) occurring on a north-dipping seismogenic zone can be traced to about a 10–20 km depth. Thus, focal mechanism solutions show P-axes orientation with the azimuth range of 340–20° by thrust events (Figure 4a). This has been revealed by the 02/04/2018 M_L 5.8 foreshock (focal mechanism P-axis 348°; 02/06 2018 M_L 6.4 mainshock; Figure 1), indicating a typical subduction zone earthquake. These images also delimited the westernmost edge of the top of the subducting PSP slab beneath a 10–20 km depth (Figure 2, transects 1–2).

There are focal mechanism solutions of 312 data points (88.4%) at a depth of

20–60 km, and around an east-dipping seismogenic zone along the westernmost edge of the PSP, showcasing P-axes orientation with the azimuth range of 280–300° by reverse and oblique-reverse (other) events (all of 353 data) (Figures 2, transects 1–2; Figures 4b and 5b). Additionally, this also corresponds to the direction of plate convergence in response to GPS observations (Chen et al., 2017a; Ching et al., 2011).

The northward subducting PSP beneath the Backbone Range has been previously identified from tomographic studies (Chemenda et al., 1997; Lin et al., 2004; Wu et al., 2007, 2009a; Chen et al., 2013, 2017a; Lallemand et al., 2013; Huang et al., 2014). Kao and Jian (2001) called this subduction a "slab-continent collision". Thus, the double wedge of Taiwan's orogen truly occurs as a result of the indentation of the PSP slab into the northern Backbone Range (Figure 6a). Therefore, the indentation tectonics have generated a west-dipping thrust of the CRF, bounding the two plates.

4.4 Lithospheric Structures of the Backbone Range

In the Backbone Range, the upper crust exhibits high velocity anomalies and low Vp/Vs that represent the compact metamorphic rocks, in the most seismically active area (Figures 2 and 3 (area-5)). Most earthquakes throughout the Backbone Range are limited to a depth of 20 km above the Conrad discontinuity (Vp < ~5.5 km/s) and rarely occur below the discontinuity within the mountain root.

With the spatial distribution of earthquakes, sharp and linear clusters are confined to the northern Backbone Range and are usually located at the sharp lateral variations of the Vp/Vs area. The earthquake clusters may be identified as individual extensional faults. Contrastingly, earthquakes are distributed rather randomly in the southern Backbone Range (Figure 3).

In the northern Backbone Range, focal mechanisms show that the recent stress field is characterized by extensional deformation observed for normal (165 data; Figures 3, 4f, and 5d) and strike-slip (7 data) events. Simultaneously, focal mechanisms in the southern Backbone Range show that the recent stress field is characterized by extensional and left-lateral transtensional deformations, which were observed for normal (173 data; Figures 3, 4f, and 5d) and strike-slip (79 data; Figure 5e) events. Normal and oblique-normal (other) focal mechanism solutions of 510 data points (88.5%) were characterized by T-axes (extension) orientations with the azimuth range from 30–60°. In addition, the rest of the strike-slip focal mechanism solutions were determined from of 86 data points (14.2%) with P- and T-axes orientation and an azimuth range of 300–330° and 30–60° (Figures 4f, 5d, and 5e), respectively. This is also consistent with the gradient tensors calculated from the continuous GPS results (Chen et al., 2017a). Apparently, the combination of these events suggests that the northern and southern Backbone Ranges are expressed by extensional and left-lateral transtensional deformations in the upper crust (< 20 km depth), respectively, indicating different tectonic activities compared to the collision zone.

From Vp velocity (Vp = 7.5 km/s) mapping, it was found that the depth of the Moho interface varies from 50–55 km beneath the Backbone Range, abruptly rising up to 25–30 km beneath the Longitudinal Valley, and to 30–40 km under the Coastal Range (Figure 2) (Rau and Wu, 1995; Kim et al, 2005, 2006; Wu et al., 2007; Kuo-Chen et al., 2012; Lallemand et al., 2013; Huang et al., 2014). The crust thickness of the Backbone Range, especially the layer below the Conrad discontinuity (Vp = ~5.5–6.5 km/s), is more than twice of the thickness on the Western Foothills (Rau and Wu, 1995; Lin et al., 1998; Kim et al., 2005; Wu et al., 2007, 2014; Kuo-Chen et al., 2012; Huang et al., 2014). Thickening and shortening in the middle-lower crust are accommodated by buckling of the upper crust in response to the collision. According to the geodetic observations in the Backbone Range, uplift and shortening rates of 6–14 and 30 mm/yr, respectively, are controlled by the bulk shortening process (Hsu et al., 2018).

4.5 Lithospheric Structures of the Collision Zone

Here, tomographic images revealed an anomalously high velocity zone beneath the Longitudinal Valley, suggesting a sudden shallowing of the PSP mantle wedge ($Vp \geq 7.5$ km/s) at a depth of about 20–30 km, which extruded within the upper crust (Kim et al., 2005, 2006; Cheng, 2009; Liang et al., 2007; Kuo-Chen et al., 2012; Wu et al., 2014). Alternatively, other studies have suggested that the existence of a high Vp zone may correspond to a remaining forearc crustal slab under the Longitudinal Valley (Cheng et al., 1998, 2002; Malavielle et al., 2002; Lallemand et al., 2013). The forearc crustal slab could be indenting the middle-lower EU crust to form a pop-up deformation of the orogenic belt (Willett and Brandon, 2002; Willett et al., 2003; Van Arendonk et al., 2014). By using sandbox modeling, an assumption was made that a west-dipping inclined backstop (forearc crust) was inserted under the Backbone Range, and led to the development of a west-dipping thrust and pop-up fold (Malavieille and Trullenque, 2009).

In this study, an observed high velocity feature with a high Vp and positive Vs perturbation structure experiences a continuous eastward distribution from the Backbone Range to below the Coastal Range (Figure 2, transects 3–10), and can also be delineated by Huang et al. (2014) in Figures 5A and 5B. In general, the high velocity perturbation represents compact rocks characterized by low porosity and the lack of fluid (Baris et al., 2005). This characteristic is well correlated with the metamorphic belt located in the Backbone Range, suggesting that the EU is subducting eastward under the Coastal Range of the PSP at this location (Carena et al., 2002; Huang et al., 2014; Wu et al., 2014). However, our tomographic images seem to be unable to significantly corroborate a forearc crust under the Backbone Range at the middle-lower crust region, or the collision zone beneath the Longitudinal Valley (Figure 6b). Chemenda et al. (1997), Malavieille et al. (2002), and McIntosh et al., (2005) alternatively inferred an active west-dipping thrust under the Coastal Rang in order to interpret the shortening of the PSP and forearc indentation, however, no definitive evidence of our relocated seismicity shows a seismogenic zone existing at this location (Figure 2, transects 3–10). As aforementioned, the west-dipping thrust of the CRF is present under the Backbone Range, which cuts through a high velocity zone (Figure 6b).

In this study, we confirmed previous interpretations of the exhumation of the forearc mantle wedge beneath the shallower collision zone in response to the collision effects (Kuo-Chen et al., 2012). However, the exhumed mantle also takes place in the NLT of the incipient collision region (Figure 2, transects 10–13). Further south of the southeast offshore, Doo et al. (2015) used a gravity model to interpret the exhumation of a serpentinized mantle wedge beneath the accretionary prism and forearc basin. Thus, the exhumed lower crustal layer (Vp > 6.0 km/s) and mantle may have been driven by indentation of the middle continental crust. This scenario would imply that the Backbone Range in the upper crust could develop the pop-up fold and accompanied by a backthrust of the CRF at the retro-wedge side. The backthrust along the eastern side of the Backbone Range has long been hypothesized and this study verified its existence. However, our tomographic images cannot identify the remaining forearc crust below the Longitudinal Valley.

The mantle wedge exhumation model is usually associated with the emplacement of high-pressure rocks at a shallow depth or the ground surface along the convergent zone (Agard et al., 2009; Liou et al., 2009; Warren, 2013). However, the eastern Backbone Range is exposed to the middle Miocene high-pressure rocks (glaucophane schist) of the Yuli belt, showcasing bears convincing evidence of the interaction between the subducted EU continent and the exhumed forearc mantle wedge during the arc-continent collision (Chen et al., 2017b). A similar process of mantle wedge overlying the subducting continental slab occurs at the Timor region of the non-volcanic outer Banda Arc where the world's youngest high-pressure metamorphic belt was outcropped during the Pliocene (Kadarusman et al., 2010).

5. Conclusions

East of Taiwan, plate convergence between the PSP and EU Plates occurs with complicated tectonic settings. In this study, we combined seismic tomography, relocated seismicity, and focal-mechanisms to assist us in delineating seismogenic zones along the convergent plate boundary. Then, we mapped two major seismogenic zones of the CRF and the LLF. There two zones are supposed to be understood crustal structures and transitioned from subduction-collision to collision zones.

However, along our transects in the southeastern offshore, the NLT of a remnant forearc basin has gradually closed while forearc crust began to descend into the convergent zone. To the north, the Longitudinal Valley has developed a completely closed forearc basin where the Coastal Range was overthrust westward onto the Backbone Range along the LVF. Thus, the development of convergent zone from the southeastern offshore to the Longitudinal Valley shows the progressed closure of the forearc basin from its incipient to mature collision, caused by the two opposite dipping thrust systems (LVF–LLF and CRF) toward each other. North of the Hualien city region, the westernmost PSP was turn subducting northward under the Backbone Range of the EU. However, tectonic features of these plate convergent regions are different but can all be characterized by the two significant opposite dipping seismogenic zones.

In this study, we first delineated the presence of the west-dipping backthrust of the CRF beneath the eastern Backbone Range in the retro-wedge province, which is shortens and uplifts the growing orogen. This backthrust acts as the Backbone Range of the pop-up fold; therefore, playing an important role in the evolution of Taiwan's orogen. Our results provide new tectonic features along the convergent zone and constraints for geodynamic models for arc-continent collisions, allowing us to investigate the current mountain building in Taiwan.

Acknowledgements

This research is funded by the MOST (grand number MOST 109-2116-M-002-023). Datasets for this research are described in these papers: the velocity model of Taiwan is from Huang et al., (2014), the relocated seismicity and the focal-mechanism of Taiwan are from Wu et al., (2008a and 2008b). The full dataset could be downloaded through the official website of the Taiwan Earthquake Research Center (TEC Data Center, TECDC; https://tecdc.earth.sinica.edu.tw/TWtomo/ModelInfo.php).

References

Agard, P., Yamato, P., Jolivet, L., and Burov, E., 2009. Exhumation of oceanic blueschists and eclogites in subduction zones: timing and mechanisms. Earth-Science Reviews 92 (1), 53–79.

Baris, S., Nakajima, J., Hasegawa, A., Honkura, Y., Ito, A., and Balamir Üćer, S., 2005. Three-dimensional structure of *Vp*, *Vs* and *Vp/Vs* in the upper crust of the Marmara region, NW Turkey. Earth Planets Space 57, 1019–1038.

Biq, C., 1965. The east Taiwan rift. Petroleum Geology of Taiwan 4, 93–106.

Carena, S., Suppe, J., and Kao, H., 2002. Active detachment of Taiwan illuminated by small earthquakes and its control of first order topography. Geology 30, 935–938.

Canitano, A., Hsu, Y.J., Lee, H.M., Linde, A.T., and Sacks, S., 2015. Near-field strain observations of the October 2013 Ruisui, Taiwan, earthquake: Source parameters and limits of very short-term strain detection. Earth Planets and Space 67, 125, DOI 10.1186/s40623-015-0284-1

Chang, P.Y., 2015. Study of the surface structure of active fault (1/4), 104-5526904000-07-01. pp. 224.

Chemenda, A.I., Yang, R.K., Hsieh, C.H., and Groholsky, A.L., 1997. Evolutionary model for the Taiwan collision based on physical modeling. Tectonophysics 274, (1–3), 253–274.

Chen, K.H., Kennett, B.L.N., and Furumura, T., 2013. High-frequency waves guided by the subducted plates underneath Taiwan and their association with seismic intensity anomalies. Journal of Geophysical Research 118, 1–16.

Chen, K.H., Wu, Y.M., Hsu, Y.J., and Chan, Y.C., 2017a. Current crustal deformation of the Taiwan orogen reassessed by cGPS strain-rate estimation and focal mechanism stress inversion. Geophysical Journal International 210, 228–239.

Chen, W.S., and Wang, Y., 1988. Development of deep-sea fan systems in Coastal Range basin, eastern Taiwan. Acta Geologica Taiwanica 26, 37–56.

Chen, W.S., Yen, I.C., Fengler, K.P., Rubin, C.M., Yang, C.C., Yang, H.C., Chang, H.C., Lin, C.W., Lin, W.H., Liu, Y.C., and Lin, Y.H., 2007. Late Holocene paleoearthquake activity in the middle part of the Longitudinal Valley fault, eastern Taiwan. Earth and Planetary Science Letters 264(3/4), 420–437.

Chen, W.S., Chung, S.L., Chou, H.Y., Zugeerbai, Z., Shao, W.Y., and Lee, Y.H., 2017b. A reinterpretation of the metamorphic Yuli belt: Evidence for a middle-late Miocene accretionary prism in eastern Taiwan. Tectonics 36, doi: 10.1002/2016TC004383

Chen, W.S., Wu, Y.M., Yeh, P.Y., Lai, Y.X., Ke, M.C., Ke, S.S., and Lin, Y.K., 2018.

Seismogenic Structures of the Eastern Taiwan Collision Zone. Special Publication, Center Geological Survey, MOEA. 33, 123–155. (in Chinese with English abstract)

Chen, W.S., Wu, Y.M., Yeh, P.Y., Lai, Y.X., Ke, M.C., Ke, S.S., and Lin, Y.K., 2019. Seismogenic Structures of the Subduction-collision Transitional Zone in Southeastern Taiwan Offshore. Special Publication, Center Geological Survey, MOEA. 34, 125–140. (in Chinese with English abstract)

Cheng, W.B., 2009, Tomographic imaging of the convergent zone in Eastern Taiwan–a subducting forearc sliver revealed? Tectonophysics 466, 170–183.

Cheng, W.B., and Wang, C.S., 2001. Seismogenic Zones in the Convergent Margin, Eastern Taiwan and Its Implications in the Luzon Forearc Deformation. Terrestrial Atmospheric and Oceanic Sciences 12, 269–286.

Cheng, W.B., Wang, C., Shyu, C.T., and Shin, T.C., 1998, A three-dimensional Vp Model of the southeastern Taiwan area and its tectonic implications. Terrestrial Atmospheric and Oceanic Sciences 9, 425–452.

Cheng, W.B., Wang, C., Shyu, C.T., and Shin, T.C., 2002. Crustal structure of the convergent plate-boundary zone, eastern Taiwan, assessed by seismic tomography, in Geology and Geophysics of an Arc-Continent Collision, Taiwan, edited by T.B. Byrne and C.S. Liu, pp. 161–175, Geological Society America Special Paper 358, Boulder, Colorado.

Ching, K.E., Hsieh, M.L., Johnson, K.M., Chen, K.H., Rau, R.J., and Yang, M., 2011. Modern vertical deformation rates and mountain building in Taiwan from precise leveling and continuous GPS observations, 2000–2008, Journal of Geophysical Research 116, B08406.

Chuang, R.Y., Johnson, K.M., Kuo, Y.T., Wu, Y.M., Chang, C.H., and Kuo, L.C., 2014. Active back thrust in the eastern Taiwan suture revealed by the 2013 Rueisuei earthquake: Evidence for a doubly vergent orogenic wedge? Geophysical Research Letters 41, 3464–3470.

Doo, W.B., Lo, C.L., Kuo-Chen, H., Brown, D,. and Hsu, S.K., 2015. Exhumation of serpentinized peridotite in the northern Manila subduction zone inferred from forward gravity modeling. Geophysical Research Letters 42, 7977-7982.

Hirtzel, J., Chi, W.C., Reed, D., Chen, L., Liu, C.S., and Lundberg, N., 2009. Destruction of Luzon forearc basin from subduction to Taiwan arc-continent collision. Tectonophysics 479, 43–51.

Ho, C.S., 1986. An Introduction to the Geology of Taiwan: Explanatory Text of the Geologic Map of Taiwan. Center Geological Survey, Taipei.

Huang, C.Y., Shyu, C.T., Lin, S.B., Lee, T.Q., and Sheu, D.D., 1992. Marine geology in the arc–continent collision zone off southeastern Taiwan: implications for late

Neogene evolution of the Coastal Range. Marine Geology 107, 183–212.

Huang, H.H., Wu, Y.M., Song, X., Chang, C.H., Lee, S.J., Chang, T.M., and Hsieh, H.H., 2014. Joint Vp and Vs tomography of Taiwan: implications for subduction-collision orogeny. Earth and Planetary Science Letters 392, 177–191.

Lallemand, S., Theunissen, T., Schnürle, P., Lee, C.S., Liu, C.S., and Font, Y., 2013. Indentation of the Philippine Sea plate by the Eurasia plate in Taiwan: details from recent marine seismological experiments. Tectonophysics 594, 60–79.

Lee, S.J., Huang, H.H., Shyu, J.B.H., Yeh, T.Y., and Lin, T.C., 2014. Numerical earthquake model of the 31 October 2013 Ruisui, Taiwan, earthquake: Source rupture process and seismic wave propagation. Journal of Asian Earth Sciences 96, 374–385.

Liang, W.T., Chiu, J.M., and Kim, K.H., 2007. Anomalous Pn waves observed in Eastern Taiwan: Implications of a thin crust and elevated oceanic upper mantle beneath the active collision-zone suture. Bulletin of the Seismological Society of America 97, 4, 1370–1377.

Lin, C.H., Yeh, Y.H., Yen, H.Y., Chen, K.C., Huang, B.S., Rocker, S., and Chiu, J.M., 1998. Three-dimensional elastic wave velocity structure of the Hualien region of Taiwan: evidence of active crustal exhumation. Tectonics 17, 1, 89–103.

Lin, J.Y., Hsu, S.K., and Sibuet, J.C., 2004. Melting features along the western Ryukyu slab edge (northeast Taiwan): Tomographic evidence. Journal of Geophysical Research 109, B12402, doi:10.1029/2004JB003260.

Liou, J.G., Ernst, W.G., Zhang, R.Y., Tsujimori, T., and Jahn, B.M., 2009. Ultrahigh-pressure minerals and metamorphic terranes–the view from China. Journal of Asian Earth Sciences 35 (3), 199–231.

Liu, T.K., Chen, Y.G., Chen, W.S., and Jiang, S.H., 2000. Rates of cooling and denudation of the early Penglai orogeny, Taiwan, as assessed by fission track constraints. Tectonophysics 320, 69–82.

Lombardi, D., Braunmiller, J., Kissling, E., and Giardini, D., 2008. Moho depth and Poisson’s ratio in the Western–Central Alps from receiver functions. Geophysical Journal International 173 (1), 249–264.

Kadarusman, A., Maruyama, S., Kaneko, Y., Ota, T., Ishikawa, A., Sopaheluwakan, J., and Omori, S., 2010. World's youngest blueschist belt from Leti Island in the non-volcanic Banda outer arc of Eastern Indonesia. Gondwana Research 18, 189–204.

Kao, H., 1998. Can great earthquakes occur in the southernmost Ryukyu arc-Taiwan region? Terrestrial Atmospheric and Oceanic Sciences 9, 487–508.

Kao, H., Shen, S.S.J., and Ma, K.F., 1998. Transition from oblique subduction to collision: Earthquakes in the southernmost Ryukyu arc-Taiwan region. Journal of Geophysical Research 103, 7211–7229.

Kao, H., and Jian, P.R., 2001. Seismogenic patterns in the Taiwan region: insights from source parameter inversion of BATS data. Tectonophysics 333, 179–198.

Kim, K.H., Chiu, J.M., Pujol, J., Chen, K.C., Huang, B.S., Yeh, Y.H., and Shen, P., 2005. Three-dimensional VP and VS structural models associated with the active subduction and collision tectonics in the Taiwan region. Geophysical Journal International 162, 204–220.

Kim, K.H., Chiu, J.M., and Chen, K.C., 2006. Polarity Reversal of Active Plate Boundary and Elevated Oceanic Upper Mantle beneath the Collision Suture in Central Eastern Taiwan. Bulletin of the Seismological Society of America 96, 3, 796–806.

Kuo, C.H., Wen, K.L., Hsieh, H.H., Lin, C.M., Chang, T.M., Kuo, K.W., 2012. Site classification and Vs30 estimation of free-field TSMIP stations using the logging data of EGDT. Eng. Geol. 129–130, 68–75.

Kuo-Chen, H., Wu, Y.M., Chang, C.H., Hu, J.C., and Chen, W.S., 2004. Relocation of the eastern Taiwan earthquakes and its tectonic implications. Terrestrial Atmospheric and Oceanic Sciences 15, 647–666.

Kuo-Chen, H., Wu, F.T., Okaya, D., Huang, B.S., and Liang, W.T., 2009. SKS/SKKS splitting and Taiwan orogeny. Geophysical Research Letters 36, L12303. http://dx.doi.org/10.1029/2009GL038148.

Kuo-Chen, H., Wu, F.T., and Rocker, S.W., 2012. Three-dimensional P velocity structures of the lithosphere beneath Taiwan from the analysis of TAIGER and related seismic datasets. Journal of Geophysical Research 117, B06306.

Malavieille, J., and Trullenque, G., 2009. Consequences of continental subduction on forearc basin and accretionary wedge deformation in SE Taiwan: insights from analogue modeling. Tectonophysics 466, 377–394.

Malavieille, J., and Konstantinovskaya, E., 2010. Impact of surface processes on the growth of orogenic wedges: Insights from analog models and case studies. Geotectonics 44, 541–558.

Malavieille, J., Lallemand, S., Dominguez, S., Deschamps, A., Lu, C.Y., Liu, C.S., and Schnürle, P., 2002. Arc-continent collision in Taiwan: New marine observations and tectonic evolution, in Geology and Geophysics of an Arc-Continent Collision, Taiwan, edited by T.B. Byrne and C.S. Liu, Geological Society America Special Paper 358, 187–211.

McIntosh, K., Nakamura, Y., Wang, T.K., Shih, R.C., Chen, A., and Liu, C.S., 2005. Crustal-scale seismic profiles across Taiwan and the western Philippine Sea. Tectonophysics 401, 23–54.

Mozziconacci, L., Delouis, B., Huang, B.S., Lee, J.C., and Béthoux, N. (2013)

Determining fault geometry from the distribution of coseismic fault slip related to the 2006 Taitung earthquake, Eastern Taiwan. Bulletin of the Seismological Society of America 103, 394–411.

Rau, R.J., and Wu, F.T., 1995. Tomographic imaging of lithospheric structures under Taiwan. Earth and Planetary Science Letters 133, 517–532.

Rau, R.J., and Wu, F.T., 1998. Active tectonics of Taiwan orogeny from focal mechanisms of small-to-moderate-sized earthquakes. Terrestrial Atmospheric and Oceanic Sciences 9, 755–778.

Shao, W.Y., Chung, S.L., Chen, W.S., Lee, H.Y., and Xie, L.W., 2015. Old continental zircons from a young oceanic arc, eastern Taiwan: Implications for Luzon subduction initiation and Asian accretionary orogeny. Geology 6, 479–482.

Shyu, J.B.H., Sieh, K., Avouac, J.P., Chen, W.S., and Chen, Y.G., 2006. Millennial slip rate of the Longitudinal Valley fault from river terraces: Implications for convergence across the active suture of eastern Taiwan. Journal of Geophysical Research 111, B08403.

Suppe, J., 1981. Mechanics of mountain building and metamorphism in Taiwan. Geological Society of China Memorial 4, 67–89.

Suppe, J., 1984. Kinematics of arc-continent collision, flipping of subduction, and back-arc spreading near Taiwan. Geological Society of China Memorial 6, 21–33.

Teng, L.S., 1990. Geotectonic evolution of late Cenozoic arc-continent collision in Taiwan. Tectonophysics 183, 57–76.

Tsai, Y.B., 1986. Seismotectonics of Taiwan. Tectonophysics 125, 17–37.

Ustaszewski, K., Wu, Y.M., Suppe, J., Huang, H.H., Chang, C.H., and Carena, S., 2010. Crust–mantle boundaries in the Taiwan–Luzon arc-continent collision system determined from local earthquake tomography and 1D models: Implications for the mode of subduction polarity reversal. Tectonophysics 578, 31–49.

Van Arendonk, Kuo-Chen, H., Mcintosh, K.D., Lavier, L., Okaya, D.A., Wu, F.T., Wang, C.Y., Lee, C.S., and Liu, C.S., 2014. Deep crustal structure of an arc-continent collision: constraints from seismic travel times in central Taiwan and the Philippine Sea. Journal of Geophysical Research: Solid Earth 119, 8397–8416.

Warren, C.J., 2013. Exhumation of (ultra-) high-pressure terranes: concepts and mechanisms. Solid Earth 4 (1), 75–92.

Wen, Y.Y., Yen, Y.T., Wen, S., Lee, S.J., Kuo, C.H., and Lin, Y.Y., 2016. Hybrid Ground Motion Simulation for the 2013 ML 6.4 Ruisui, Taiwan Earthquake. Terrestrial Atmospheric and Oceanic Sciences 27, 3, 407–414.

Willett, S.D., and Brandon, M.T., 2002. On steady states in mountain belt. Geology 30, 175–178.

Willett, S. D., Fisher, D., Fuller, C., Yeh, E.C., and Lu, C.Y., 2003. Erosion rates and orogenic-wedge kinematics in Taiwan inferred from fission-track thermochronometry. Geology 31(11), 945–948.

White, R.S., McKenzie, D., and Ònions, R.K., 1992. Oceanic crustal thickness from seismic measurements and rare earth element inversions. Journal of Geophysical Research 97, 19683–19715.

Wu, F.T., Rau, R.J., and Salzberg, D., 1997. Taiwan orogeny: Thin-skinned or lithospheric collision? Tectonophysics 274, 191–220.

Wu, F.T., Liang, W.T., Lee, J.C., Benz, H., and Villasenor, A., 2009a. A model for the termination of the Ryukyu subduction zone against Taiwan: a junction of collision, subduction/separation, and subduction boundaries. Journal of Geophysical Research 114, B07404.

Wu, F.T., Kuo-Chen, H., and McIntosh, K.D., 2014. Subsurface imaging, TAIGER experiments and tectonic models of Taiwan. Journal of Asian Earth Sciences 90, 173–208.

Wu, Y. M., Chang, C.H., Hsiao, N.C., and Wu, F.T., 2003. Relocation of the 1998 Rueyli, Taiwan, earthquake sequence using three-dimensions velocity structure with stations corrections. Terr. Atmos. Ocean. Sci. 14, 421-430.

Wu, Y.M., Chen, Y.G., Chang, C.H., Chung, L.H., Teng, T.L., Wu, F.T., and Wu, C.F., 2006. Seismogenic structure in a tectonic suture zone: With new constraints from 2006 Mw 6.1 Taitung earthquake. Geophysical Research Letters 33, L22305.

Wu, Y.M., Chang, C.H., Zhao, L., Shyu, J.B.H., Chen, Y.G., Sieh, K., and Avouac, J.P., 2007. Seismic tomography of Taiwan: Improved constraints from a dense network of strong motion stations. Journal of Geophysical Research 112, B08312.

Wu, Y.M., Chang, C.H., Zhao, L., Teng, T.L., and Nakamura, M., 2008a. A comprehensive relocation of earthquakes in Taiwan from 1991 to 2005, Bull. Seism. Soc. Am., 98, 1471–1481, doi: 10.1785/0120070166.

Wu, Y.M., Zhao, L., Chang, C.H., and Hsu, Y.J., 2008b. Focal mechanism determination in Taiwan by genetic algorithm, Bull. Seism. Soc. Am. 98, 651–661, doi: 10.1785/0120070115.

Wu, Y.M., Shyu, J.B.H., Chang, C.H., Zhao, L., Nakamura, M., and Hsu S.K., 2009b. Improved seismic tomography offshore northeastern Taiwan: Implications for subduction and collision processes between Taiwan and the southernmost Ryukyu. Geophysical Journal International 178, 1042–1054.

Wu, Y.M., Hsu, Y.J., Chang, C.H., Teng, L.S., and Nakamura, M., 2010. Temporal and spatial variation of stress field in Taiwan from 1991 to 2007: Insights from comprehensive first motion focal mechanism catalog. Earth and Planetary Science Letters 298, 306–316, doi: 10.1016/j.epsl.2010.07.047.

Wu, Y.M., Chang, C.H., Kuo-Chen, H., Huang, H.H., and Wang, C.Y., 2013. On the use of explosion records for examining earthquake location uncertainty in Taiwan. Terr. Atmos. Ocean. Sci. 24, 685-694, doi: 10.3319/TAO.2013.01.31.01(T).

Yen, T.P., 1967. Structural analysis of the Tananao Schist of Taiwan. Bulletin of the Geological Survey, Taiwan 18, l–110.

Yen, I.C., 2017, The progressive study of active faults in eastern Taiwan of 2017. Report of Central Geological Survey, MOEA, 49 pp. (in Chinese with English abstract)

Yui, T.F., and Chu H.T., 2000. Possible factors affecting the topography of the Backbone Range of Taiwan. Western Pacific Earth Sciences 2, 105–118.

Figure 1. 1990 to 2018 earthquake (blue dots) and historical earthquake (star marks, M>5.8) distribution map and tectonic map of the eastern Taiwan. Location of thirteen seismic tomography transects across the convergent zone of three tectonic regimes. NLA, North Luzon Arc (orange color); EU, Eurasian Plate; PSP, Philippine Sea Plate (purple color).

Figure 2. Tomographic result of Vp, Vp/Vs, and Vs perturbation structures and combine with relocated earthquakes and focal mechanisms (see Figure 1 for location). Black curve line represents the Moho interface (Vp =7.5 km/s). Red lines a, b, c, d, e represent the Central Range Fault, Longitudinal Valley Fault, Luyeh Fault, Ludao–Lanyu Fault, and Manila subduction zone, respectively. BR, Backbone Range; CR, Coastal Range; NLA, North Luzon Arc; NLT, North Luzon Trough; RT, Ryukyu Trench.

Figure 3. Map view of focal mechanisms from 1990 to 2018 (M>4) in Area 1–6. Focal mechanisms are plotted in the order of reverse (red), normal (green), and strike-slip (blue). EU, Eurasian Plate; PSP, Philippine Sea Plate (purple color).

Figure 4. Stress inversion and focal plane results, rose diagrams for the plunge angle and azimuth of the slip lines.

Figure 5. Orientation of P- (red) and T- (green) axes of focal mechanism solutions shown in Area 1–6. Focal mechanisms from 1990 to 2018 (M>4).

Figure 6. Schematic block diagrams illustrating the tectonic structures across the convergent zone in the eastern Taiwan. (a) the Ryukyu Trench subduction zone at the westernmost edge of PSP (transect 2), (b) the collision zone at the Longitudinal Valley (transect 5), (c) the collision-subduction transition zone at the southeastern offshore (transect 11). Label a, b, d, e see Figure 2.

Figure 7. Geomorphic map of the late Pleistocene–Holocene alluvial fans and river terraces, and fault trace of the Longitudinal Valley Fault (LVF), Luyeh Fault (LYF), and Central Range Fault (CRF). Transects 3–10 cross perpendicular to the LVF, LYF, and CRF (see Figure 1 for location). The dashed line represents blind fault map under the Longitudinal Valley. Label a, t, l represent Holocene alluvial fan, Holocene river terrace, and late Pleistocene lateritic terrace, respectively.

Figure 1.

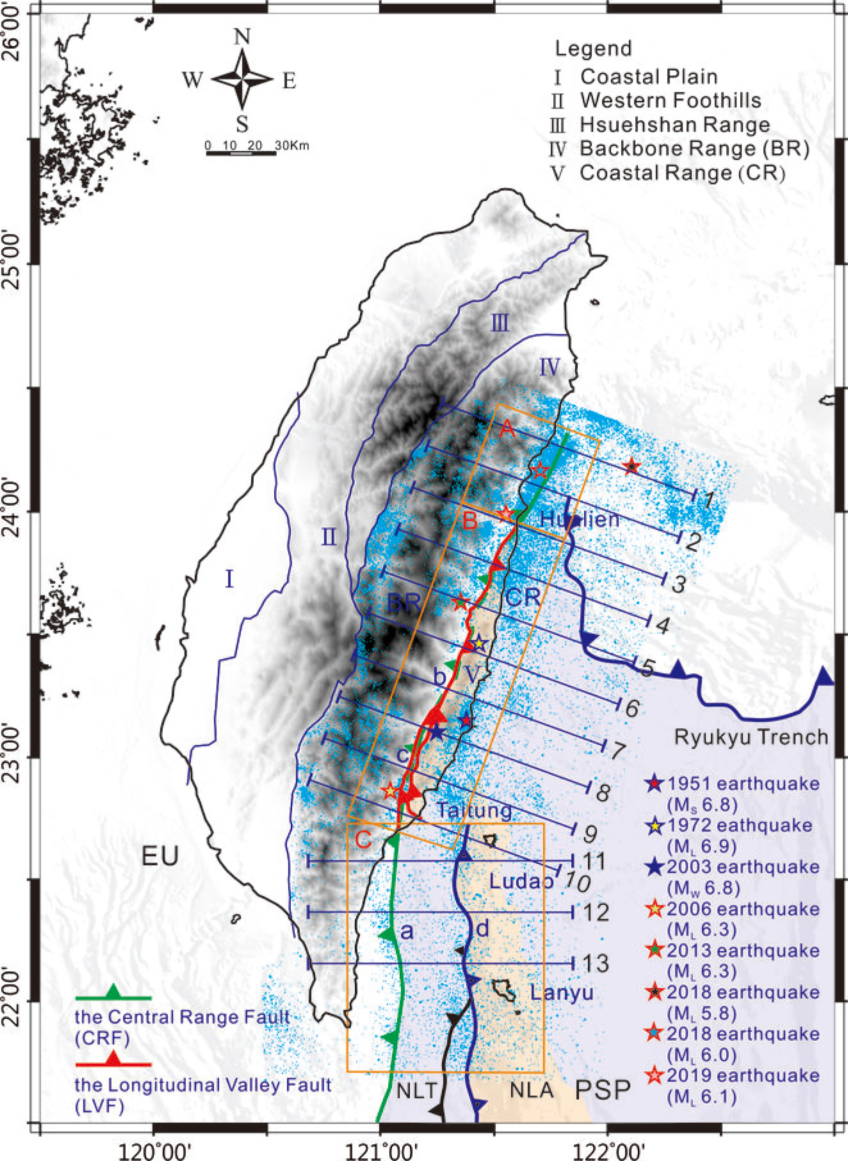

26°00'
25°00'
24°00'
23°00'
22°00'
120°00'
121°00'
122°00'
N
W
E
S
0 10 20 30Km
Legend
I Coastal Plain
II Western Foothills
III Hsuehshan Range
IV Backbone Range (BR)
V Coastal Range (CR)
III
IV
II
I
A
B
C
1
2
3
4
5
6
7
8
9
10
11
12
13
Hualien
BR
CR
V
b
c
a
d
Taitung
Ludao
Lanyu
EU
PSP
NLT
NLA
Ryukyu Trench
1951 earthquake (M_S 6.8)
1972 eathquake (M_L 6.9)
2003 earthquake (M_W 6.8)
2006 earthquake (M_L 6.3)
2013 earthquake (M_L 6.3)
2018 earthquake (M_L 5.8)
2018 earthquake (M_L 6.0)
2019 earthquake (M_L 6.1)
the Central Range Fault (CRF)
the Longitudinal Valley Fault (LVF)

Figure 2a.

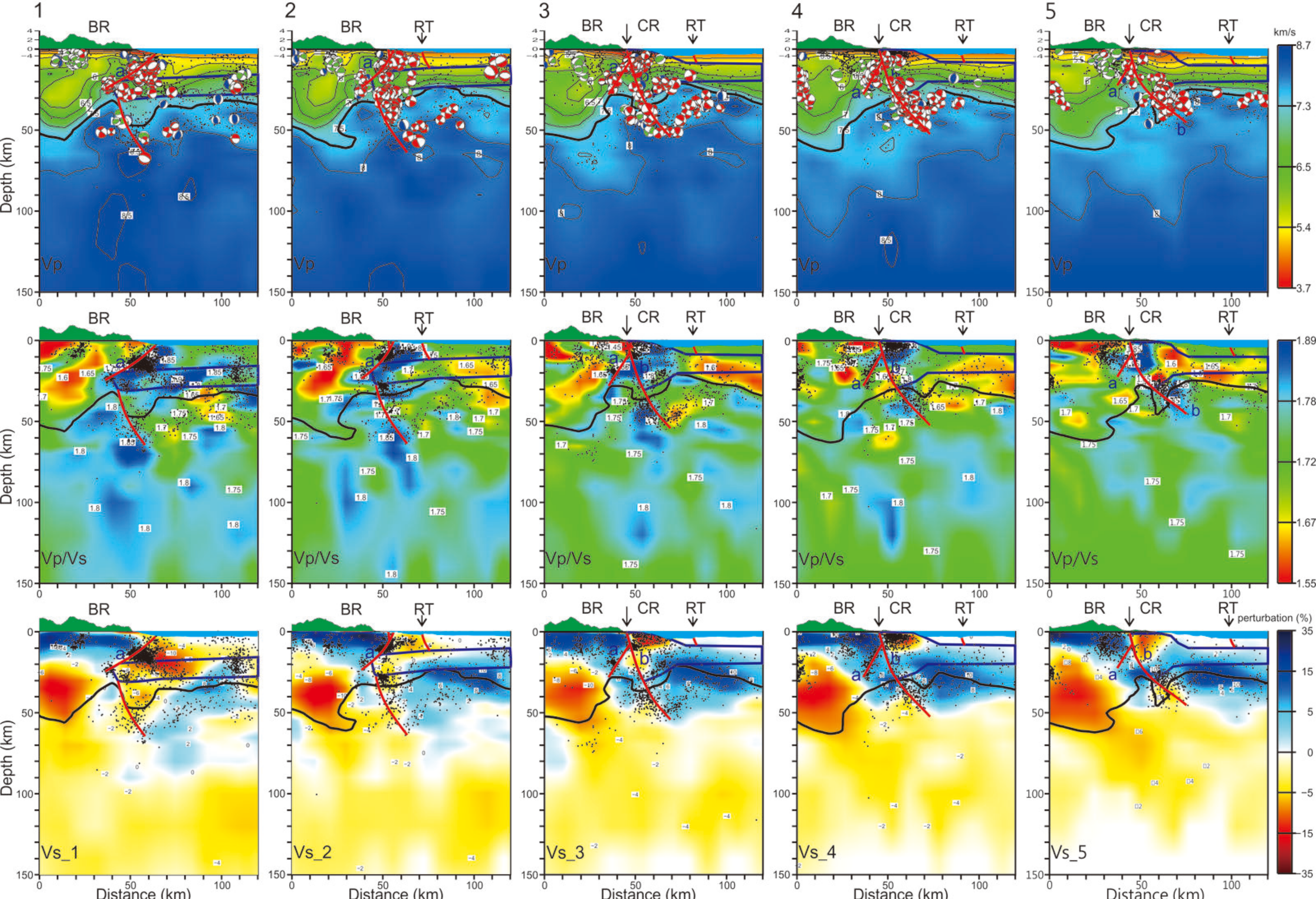

1
2
3
4
5
BR
CR
RT
a
b
Vp
Vp/Vs
Vs_1
Vs_2
Vs_3
Vs_4
Vs_5
Depth (km)
Distance (km)
km/s
perturbation (%)

Figure 2b.

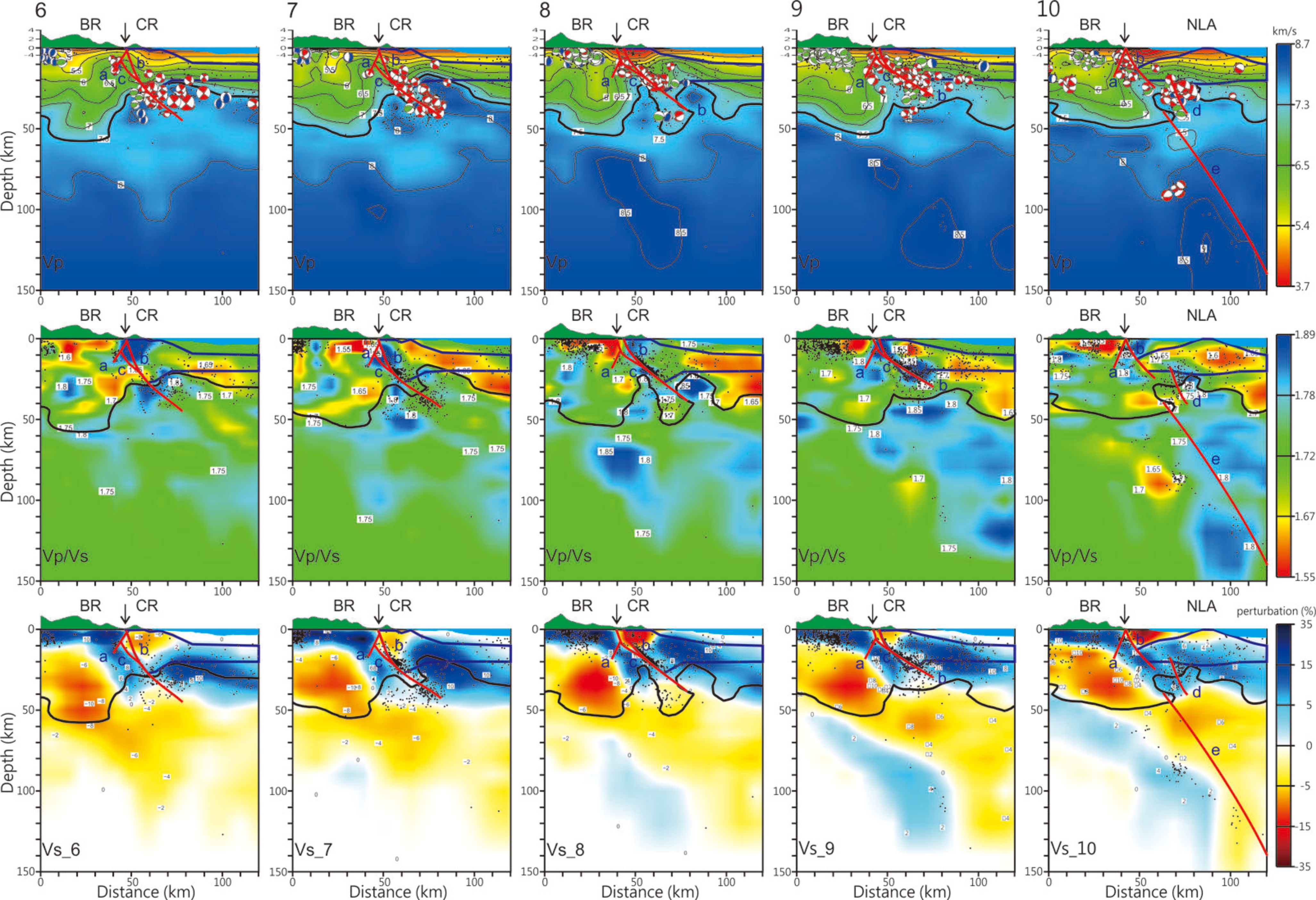

6
7
8
9
10
BR
CR
NLA
Vp
Vp/Vs
Vs_6
Vs_7
Vs_8
Vs_9
Vs_10
Depth (km)
Distance (km)
km/s
8.7
7.3
6.5
5.4
3.7
1.89
1.78
1.72
1.67
1.55
perturbation (%)
35
15
5
0
-5
-15
-35

Figure 2c.

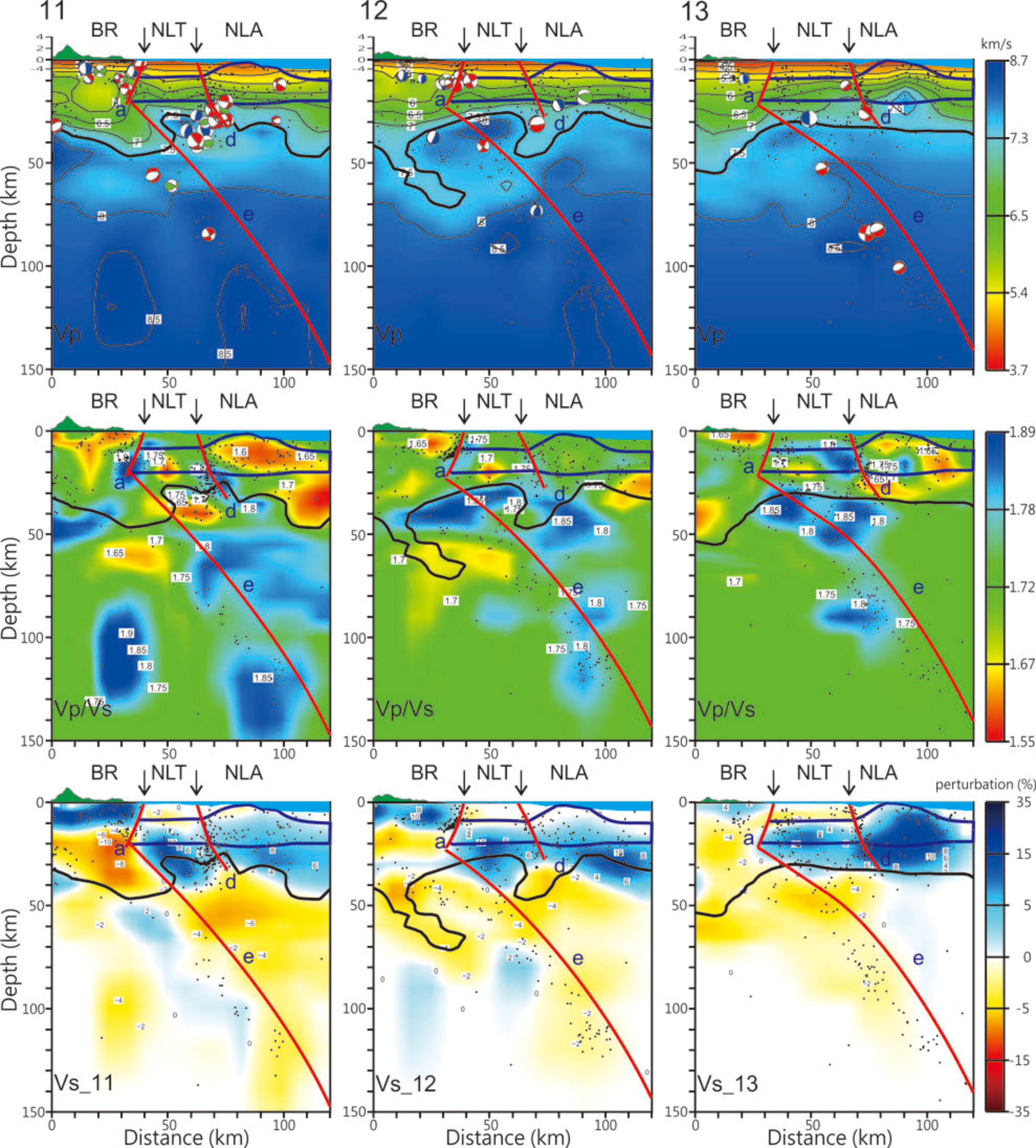

11
12
13
BR
NLT
NLA
km/s
perturbation (%)
Depth (km)
Distance (km)
Vp
Vp/Vs
Vs_11
Vs_12
Vs_13
a
d
e

Figure 3.

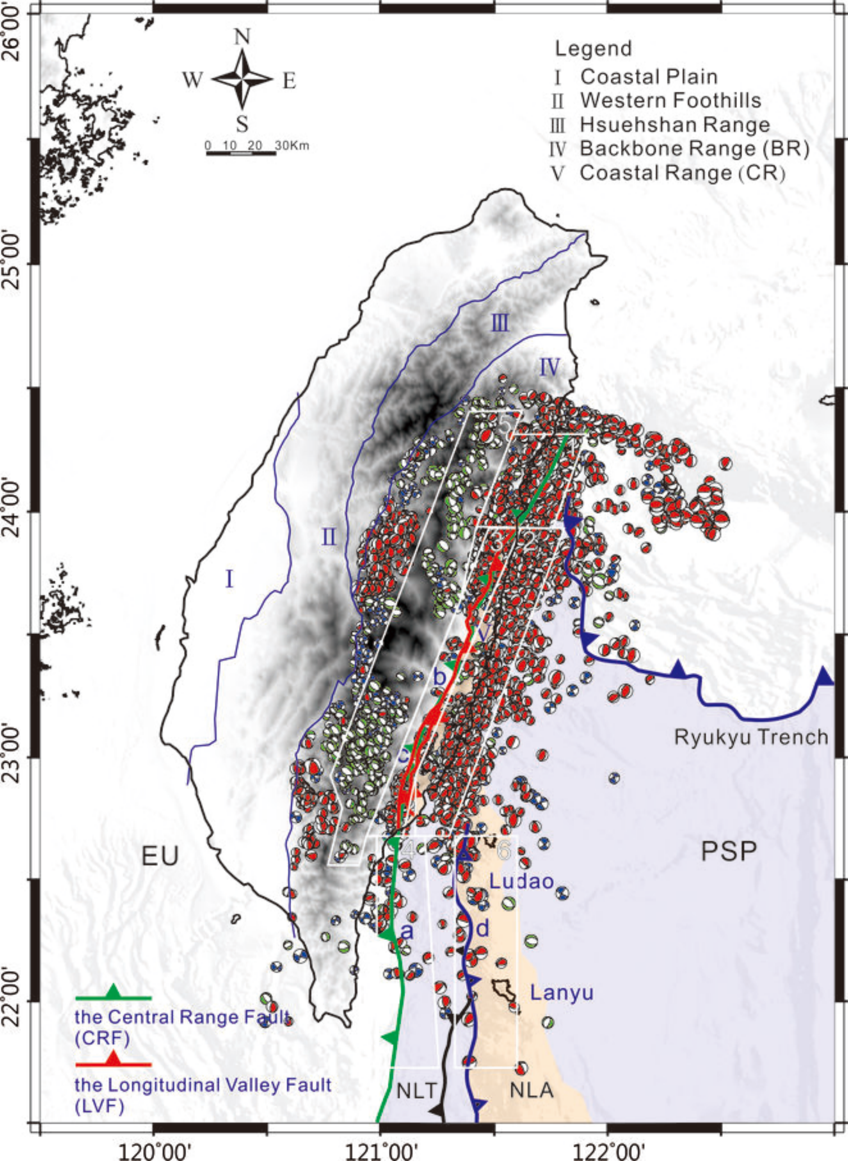

Legend
I Coastal Plain
II Western Foothills
III Hsuehshan Range
IV Backbone Range (BR)
V Coastal Range (CR)
N
S
W
E
0 10 20 30Km
26°00'
25°00'
24°00'
23°00'
22°00'
120°00'
121°00'
122°00'
I
II
III
IV
V
a
b
c
d
1
2
3
4
5
6
Ryukyu Trench
EU
PSP
Ludao
Lanyu
NLT
NLA
the Central Range Fault (CRF)
the Longitudinal Valley Fault (LVF)

Figure 4.

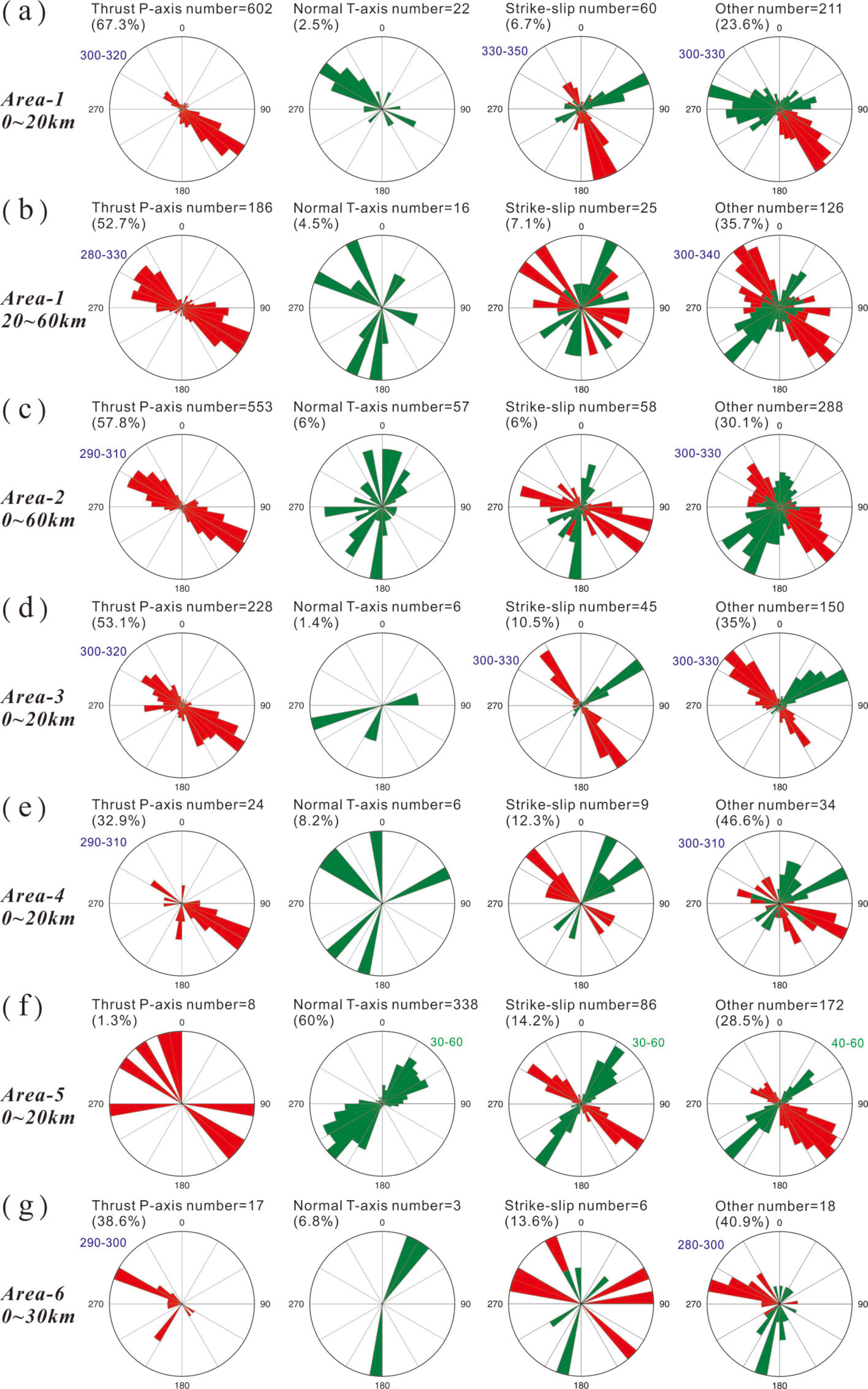

(a)
Area-1 0~20km
Thrust P-axis number=602 (67.3%)
300-320
Normal T-axis number=22 (2.5%)
Strike-slip number=60 (6.7%)
330-350
Other number=211 (23.6%)
300-330
(b)
Area-1 20~60km
Thrust P-axis number=186 (52.7%)
280-330
Normal T-axis number=16 (4.5%)
Strike-slip number=25 (7.1%)
Other number=126 (35.7%)
300-340
(c)
Area-2 0~60km
Thrust P-axis number=553 (57.8%)
290-310
Normal T-axis number=57 (6%)
Strike-slip number=58 (6%)
Other number=288 (30.1%)
300-330
(d)
Area-3 0~20km
Thrust P-axis number=228 (53.1%)
300-320
Normal T-axis number=6 (1.4%)
Strike-slip number=45 (10.5%)
300-330
Other number=150 (35%)
300-330
(e)
Area-4 0~20km
Thrust P-axis number=24 (32.9%)
290-310
Normal T-axis number=6 (8.2%)
Strike-slip number=9 (12.3%)
Other number=34 (46.6%)
300-310
(f)
Area-5 0~20km
Thrust P-axis number=8 (1.3%)
Normal T-axis number=338 (60%)
30-60
Strike-slip number=86 (14.2%)
30-60
Other number=172 (28.5%)
40-60
(g)
Area-6 0~30km
Thrust P-axis number=17 (38.6%)
290-300
Normal T-axis number=3 (6.8%)
Strike-slip number=6 (13.6%)
Other number=18 (40.9%)
280-300
0
90
180
270

Figure 5.

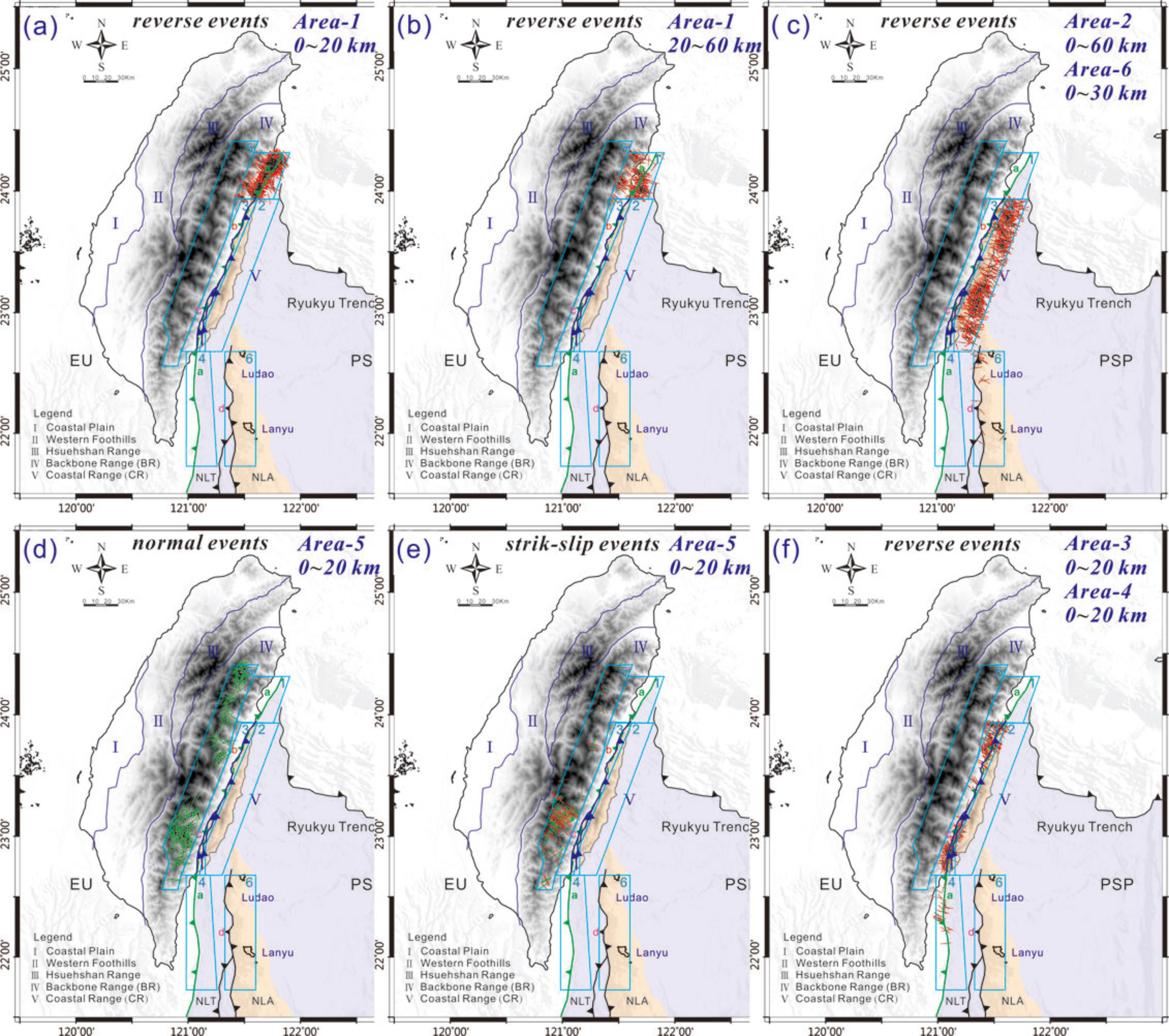

(a) reverse events Area-1 0~20 km
(b) reverse events Area-1 20~60 km
(c) reverse events Area-2 0~60 km Area-6 0~30 km
(d) normal events Area-5 0~20 km
(e) strik-slip events Area-5 0~20 km
(f) reverse events Area-3 0~20 km Area-4 0~20 km
N W E S
0 10 20 30Km
I II III IV V
Ryukyu Trench
EU
PSP
Ludao
Lanyu
NLT
NLA
Legend
I Coastal Plain
II Western Foothills
III Hsuehshan Range
IV Backbone Range (BR)
V Coastal Range (CR)
120°00' 121°00' 122°00'
22°00' 23°00' 24°00' 25°00'

Figure 6.

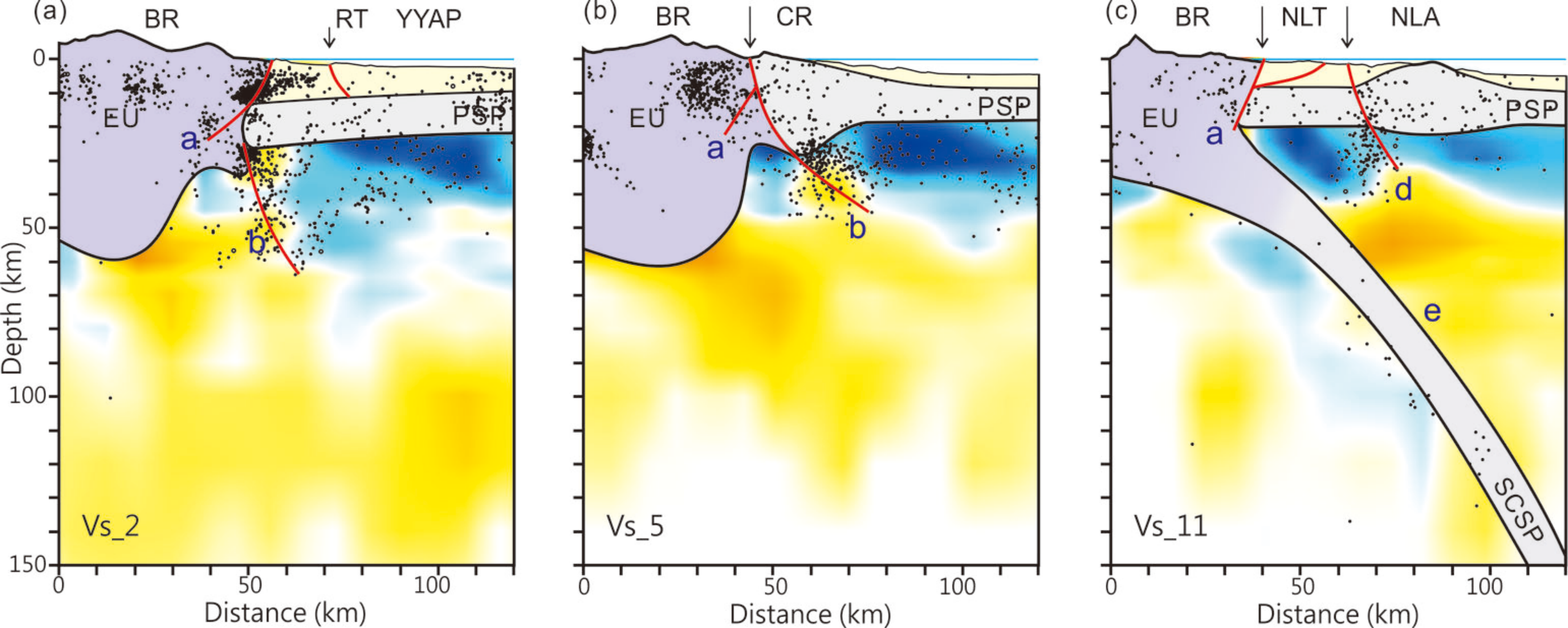

(a)
BR
RT
YYAP
EU
PSP
a
b
Vs_2
(b)
BR
CR
EU
PSP
a
b
Vs_5
(c)
BR
NLT
NLA
EU
PSP
a
d
e
SCSP
Vs_11
Depth (km)
Distance (km)
0
50
100
150

Figure 7.

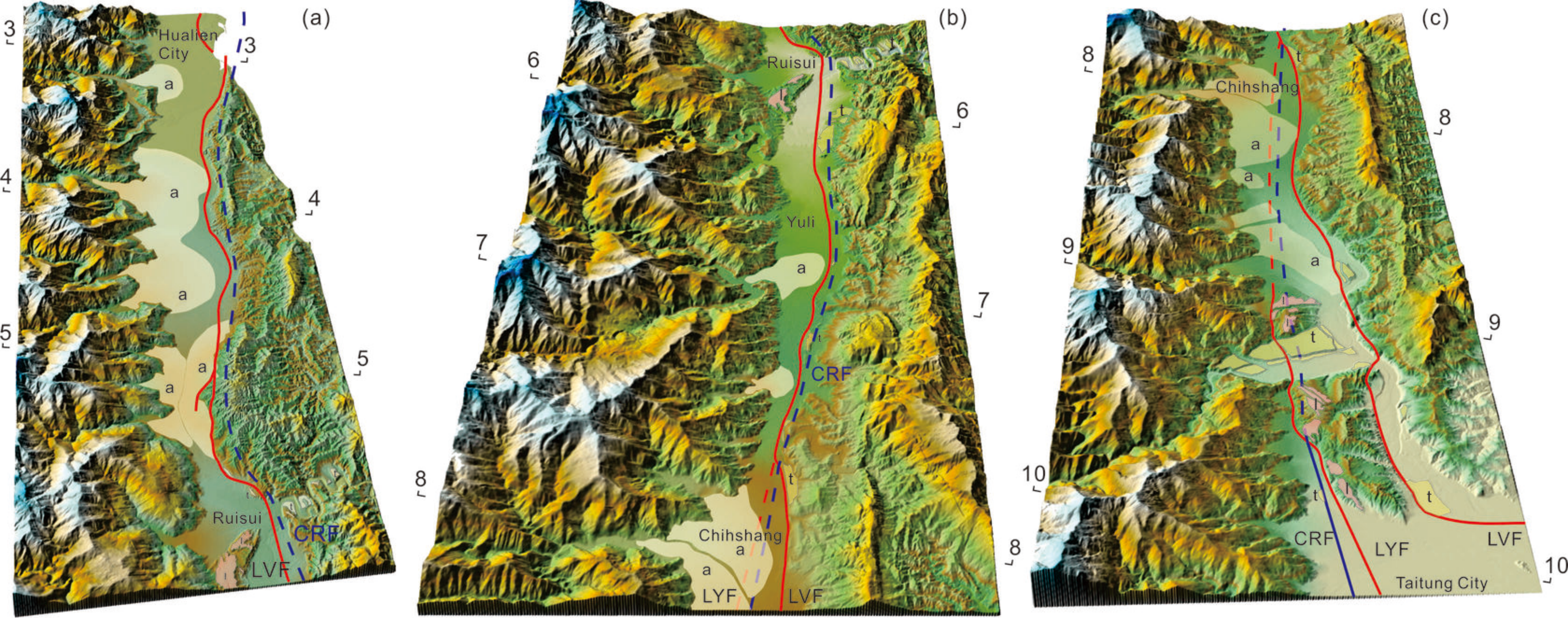
(a)
Hualien City
Ruisui
CRF
LVF
(b)
Ruisui
Yuli
CRF
Chihshang
LYF
LVF
(c)
Chihshang
CRF
LYF
LVF
Taitung City